npj Computational Materials

https://doi.org/10.1038/s41524-026-01976-4

Article in Press

Incongruent melting and phase diagram of SiC from machine learning molecular dynamics

Received: 28 October 2025

Accepted: 16 January 2026

Cite this article as: Xie, Y., Wang, M., Ramakers, S. *et al.* Incongruent melting and phase diagram of SiC from machine learning molecular dynamics. *npj Comput Mater* (2026). https://doi.org/10.1038/s41524-026-01976-4

Yu Xie, Menghang Wang, Senja Ramakers, Frans Spaepen & Boris Kozinsky

Incongruent Melting and Phase Diagram of SiC from Machine Learning Molecular Dynamics

Yu Xie[*,†,1], Menghang Wang[*,1], Senja Ramakers[2,3], Frans Spaepen[1], and Boris Kozinsky[†,1,4]

[1]John A. Paulson School of Engineering and Applied Sciences, Harvard University, Cambridge, MA 02138, USA
[2]Ruhr-Universität Bochum, Bochum, 44801, Germany
[3]Robert Bosch GmbH, Gerlingen, 70839, Germany
[4]Robert Bosch Research and Technology Center, Watertown, MA 02472, USA

Abstract

Silicon carbide (SiC) is an important technological material, but its high-temperature phase diagram has remained unclear due to conflicting experimental results about congruent versus incongruent melting. Here, we employ large-scale machine learning molecular dynamics (MLMD) simulations to gain insights into SiC decomposition and phase transitions. Our approach relies on a Bayesian active learning workflow to efficiently train an accurate machine learning force field on density functional theory data. Our large-scale simulations provide direct indication that melting of SiC proceeds incongruently via decomposition into silicon-rich and carbon phases at high temperature and pressure. During cooling at high pressures, carbon nanoclusters nucleate and grow within the homogeneous molten liquid. During heating, the decomposed mixture reversibly transitions back into a homogeneous SiC liquid. The full pressure-temperature phase diagram of SiC is systematically constructed using MLMD simulations, providing new understanding of the nature of phases, resolving long-standing inconsistencies from previous experiments and yielding technologically relevant implications for processing and deposition of this material.

[*]Equal contribution. Yu Xie conducted this work at Harvard before joining Microsoft.
[†]Corresponding to: yuxie1@microsoft.com, bkoz@seas.harvard.edu

Introduction

Silicon carbide (SiC) is an important technological material valued for its high hardness, mechanical strength, high thermal conductivity, and wide band gap [1]. The high-temperature and high-pressure behavior of SiC is of great scientific interest for understanding planetary interiors and stellar processes, due to its identification from absorption spectroscopy of carbon-rich extrasolar planets [2]. Understanding the properties of SiC under extreme conditions is also crucial for various applications, including nuclear reactors [3], epitaxial deposition growth of SiC [4, 5], and graphene synthesis [6] for electronics and quantum devices.

The melting and decomposition of SiC have been investigated by experimental and computational methods for decades. However, various experiments have reached inconsistent conclusions and thereby raised confusion about the nature of melting of SiC. Experiments at high temperatures and pressures are challenging because it is difficult to directly observe the kinetics of melting, and factors such as sample size and purity, and thermal gradients causing temperature inhomogeneity can further complicate interpretations. Moreover, internal inconsistencies within individual studies and substantial disagreement between independent measurements indicate that the experimental picture remains under-established.

In some studies, incongruent melting has been reported, with the observation that SiC decomposes into a silicon-rich liquid and solid carbon upon heating [7, 8, 9, 10]. Reported incongruent melting (decomposition) onset temperatures span a broad range: multiple sets of measurements near 10 GPa cluster in the 2800–3500 K range [7, 8, 10, 11, 12], whereas a high-pressure, laser-heated diamond-anvil cell (DAC) study [9] reports substantially lower decomposition temperatures ($\sim$ 2000 K), creating a discontinuity with the lower-pressure results. This dispersion, compounded by conflicting reports of congruent melting [13, 14], highlights that the SiC decomposition phase boundary remains experimentally under-determined and motivates a qualitative and quantitative re-examination.

Molecular dynamics (MD) simulations using density functional theory (*ab initio* MD, or AIMD) and various empirical potentials were employed to investigate the melting process of SiC. AIMD studies [15, 16] do not reach extended Si-rich/C-rich phase separation, although at the highest reported

temperature (11,000 K) the C–C peak in the radial distribution function (RDF) begins to overtake the Si–C peak, indicating substantial carbon clustering and reduction of silicon-carbon mixing. This captures the qualitative tendency toward decomposition, but the need for unrealistically high temperature together with limited cell size and timescale prevents quantitative determination of the true decomposition boundary or formation of fully phase-separated domains. On the other hand, empirical potentials, such as the Vashishta potential [17], the Tersoff potential [18, 19, 20], and the Gao-Weber potential [21], provide differing descriptions of uncertain accuracy. For example, simulations using the Vashishta potential show no formation of C-C bonds in either liquid or amorphous SiC (see Supplementary Information Fig. S3). Similarly, the Tersoff potentials [18, 19], the Gao-Weber potential [21], and a recent Behler-Parrinello neural network potential [22] studied the melting of SiC at high temperature and low to moderate pressure (0–10 GPa), showing RDF characteristics where Si-C bonds dominate, with minor C-C bonds signatures. More recent SiC ML interatomic potentials target relevant phenomena, including a UF3 model for high-temperature surface sublimation at near-ambient pressures [23] and a deep learning potential optimized for irradiation damage cascades [24]. However, they are not designed or validated for the extended high-pressure (> 10 GPa) solid-liquid decomposition transformations. Therefore, the decomposition and phase separation in the amorphous phase of SiC and its melting process remain underexplored and inconsistent across *ab initio*, empirical, and machine learning atomistic simulations, as well as experimental observations.

To overcome the limitations of previous studies, we employ a machine learning force field (MLFF) trained on density functional theory (DFT) data. First, we collect DFT data for different SiC phases and train an MLFF to describe atomic interactions using a hierarchical Bayesian active learning workflow. This approach efficiently explores the phase space across different temperatures, pressures, and compositions. Then, we perform large-scale molecular dynamics simulations, enabled by GPU acceleration, to reliably model the melting and decomposition of SiC at a sufficient scale. By conducting two-phase coexistence simulations, where the interface between two phases of interest is created and equilibrated, we quantitatively determine, for the first time, the temperatures and pressures of transitions between phases.

Our simulations provide strong evidence for incongruent melting at high pressure and offer insights into the mechanism of SiC decomposition into Si and C rich phases. The transition temperatures between the zinc-blende SiC, decomposed incongruent mixture, and the homogeneous liquid phase are identified by our simulations, at pressures ranging from 10 GPa to 120 GPa. We obtain the pressure-temperature phase diagram depicting the stability regions of different phases. Notably, our findings of the decomposition indicate that amorphous SiC can only be produced through irradiation, and not via melt-quench processes [25]. Our atomic-level results provide microscopic insights into the decomposition and melting behavior of this technologically important material, resolving discrepancies in previous experimental and computational studies.

Results

Bayesian active learning of machine learning force field

Our MLFF is based on Gaussian process regression, which provides both force predictions and per-atom uncertainty estimates [26, 27]. This enables a Bayesian active learning workflow (Fig. 1a) where MD simulations are propagated with the current surrogate, and configurations whose uncertainties exceed a threshold trigger single-point DFT queries for training data collection and surrogate update. As described in more detail in the *Methods* section, the MLFF was iteratively refined via Bayesian active learning to ensure accuracy across the phase space, while allowing us to simulate large systems efficiently. We performed multiple Bayesian active learning trajectories in parallel for different compositions (pure Si, pure C, and SiC) at various temperatures and pressures (Fig. 1b).

While a 64-atom cell is insufficient to capture decomposition, the larger 512-atom supercell enables observation of the phase separation process. As shown in Fig. 1d, the first Si-rich and C-rich domains emerged spontaneously at 30 GPa during unbiased high-T / high-P active learning MD, prior to any decomposed structures being present in the training set. We did not seed or impose this Si and C phase separation. Instead, trajectories were advanced with the current surrogate, and single-point DFT labels were added only when Bayesian force uncertainties on naturally visited

clustered configurations exceeded the acquisition threshold. This procedure preserves high-fidelity force predictions on-the-fly and expands the training set into newly accessed regions of configuration space. Consequently, the database expanded to include Si-rich and C-rich regimes solely through the natural evolution of the system's dynamics. This spontaneous appearance provides independent evidence that incongruent melting (decomposition) occurs without being assumed *a priori*, even in modest cell sizes.

Nevertheless, the phase separation observed in the 512-atom active learning simulations does not provide comprehensive information about the decomposition process. For instance, the limited cell size is insufficient to reveal whether the C and Si clusters form crystalline or liquid phases, or to determine the precise conditions under which decomposition occurs. To *qualitatively* characterize the nature of these phases and their structural properties, we perform large-scale MD simulations with up to 512,000 atoms (Fig. 2). Furthermore, to *quantitatively* determine the precise phase transition temperatures and pressures, we employ two-phase coexistence simulations (Fig. 3 and Fig. 4).

Incongruent melting from large-scale MD

Starting with the well-trained MLFF model, we run large-scale heating and cooling simulations at 30, 60, and 80 GPa to *qualitatively* characterize the nature of the phase transformation and decomposition of SiC. We start with a 512,000-atom bulk crystal supercell of the cubic zinc-blende (ZB/3C/B3) phase. At these pressures, decomposition does not occur readily during the MD simulations due to hysteresis, even when heating the cubic ZB crystal structure to temperatures as high as 4000 K. The crystal structure is only destroyed when the temperature is increased to 5000 K.

At 5000 K, across 30, 60, and 80 GPa, small separate carbon and silicon clusters form in the amorphous configurations, which indicates a trend away from a homogeneous mixture of silicon and carbon. Even though the temperature is significantly higher than experimentally reported incongruent or congruent melting points [7, 8, 9, 10, 11], the complete phase separation of C and Si does not occur. Upon cooling the system to 3000 K, we observe decomposition into carbon crystals and silicon liquid. Specifically, as the temperature drops below 4000 K, carbon clusters start to grow

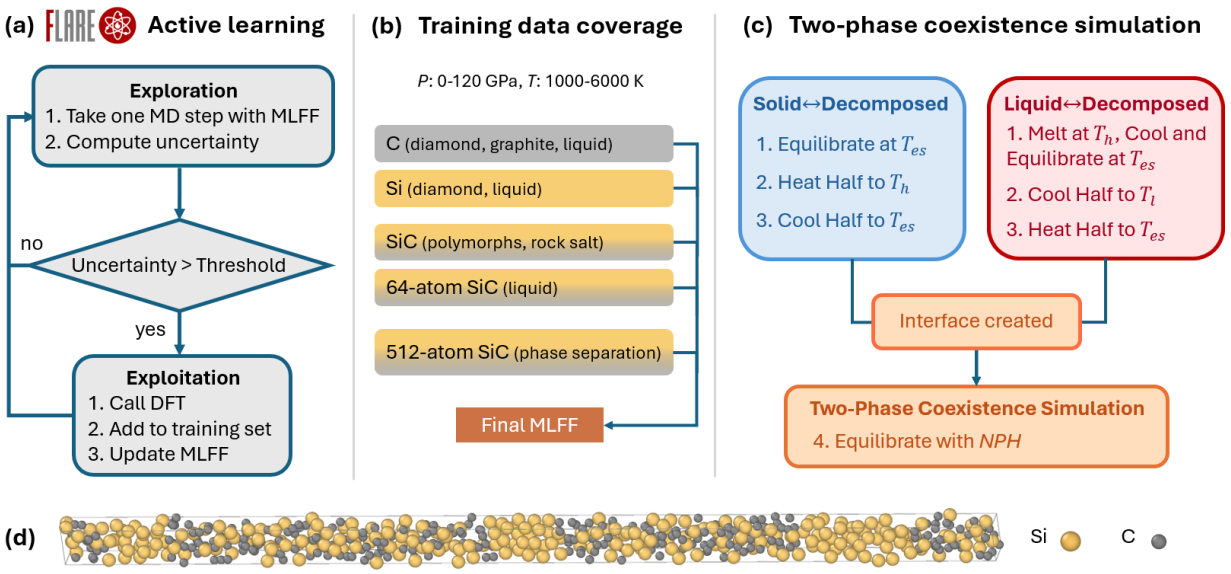

Figure 1: **Overview of active learning workflow, training data coverage, and two-phase simulation protocol** (a) Bayesian active learning workflow for collecting DFT training data on the fly during MD simulations. The MLFF predicts forces and uncertainties; configurations exceeding the uncertainty threshold trigger DFT labeling. (b) Training data composition and coverage. Multiple Bayesian active learning trajectories were performed in parallel for different compositions (pure Si, pure C, and SiC) across various temperatures and pressures. For SiC, we started with a 64-atom supercell and then extended to a 512-atom supercell where phase separation spontaneously occurred. (c) Two-phase simulation protocol to determine phase transition temperatures. Interfaces between the solid/liquid and decomposed phases were created by inducing decomposition, followed by a two-phase coexistence simulation in the NPH ensemble to converge on the final transition temperature. (d) Spontaneous decomposition during active learning. The collected data includes states where SiC decomposition occurred spontaneously during the active learning MD simulations, prior to any decomposed structures being present in the training set.

in size, while the Si concentration in the liquid phase increases. Upon further cooling to 3000 K, larger C clusters consisting of recognizable graphite or diamond crystal structure form within the Si-rich liquid.

The formation of either graphite or diamond C phases depends on the simulation pressure. The C clusters are classified as graphite-like or diamond-like structures by the polyhedral template matching [28] implemented in OVITO [29]. At 30 GPa, C clusters form graphite-like honeycomb lattice structures, while the Si-rich liquid persists throughout our simulation temperature range (3000–5000 K), which is higher than the Si melting point (1684 K at 0 GPa [30]). At 60 GPa, the

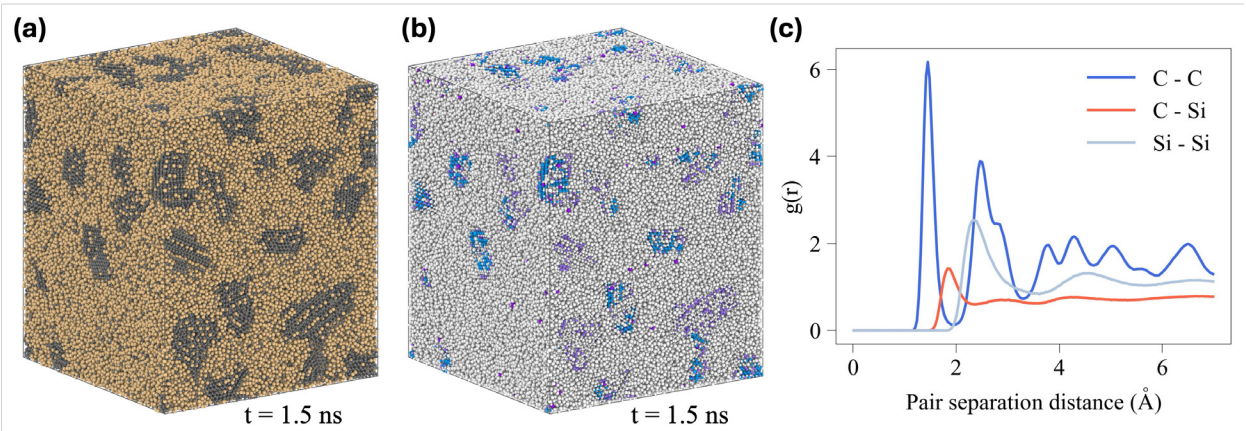

Figure 2: **Large-scale MD simulation of SiC decomposition at 60 GPa.** (a) Decomposed configuration of 512,000 atoms at the end of the simulation at 3000 K and 60 GPa. Yellow: Si, black: C. (b) Atoms colored with lattice type classified by polyhedral template matching. Blue: cubic diamond, orange: hexagonal diamond, purple: graphite, white: others. (c) Radial distribution function of the structure shows the C-C peak dominates over the Si-C peak.

diamond and graphite-like clusters incorporate Si atoms within them, as illustrated in Fig. 2b. In addition, the C-C pair distribution function exhibits a dominant peak around 1.5 Å, while the C-Si peak decreases. At 80 GPa, the decomposition results in the separation of diamond C, liquid Si, and the high-pressure rock-salt (RS/B1) phase of SiC. We have included the configurations at 30 GPa and 80 GPa and more structural analysis details in Supplementary Information Fig. S5 and S6.

Our results agree with a recent experimental observation [9] that solid C and liquid Si form upon melting (i.e., incongruent melting) of SiC at high pressures. At 120 GPa, the zinc blende to rock salt phase transition occurs, and the high pressure stabilizes the crystal structure and prevents amorphization, with no liquid phase appearing up to 5000 K.

In the next sections, we quantitatively determine the transition temperatures between the crystalline, decomposed, and homogeneous liquid phases using two-phase coexistence simulations, and build the P-T phase diagram of SiC.

High-temperature phase boundary: decomposed Si+C ↔ homogeneous liquid

Having established that decomposition occurs, we next explore the phase transition between the decomposed and homogeneous liquid states. To verify the reversibility of the incongruent

high-pressure melting and to quantitatively identify the transition temperature and pressure of the spontaneous decomposition, we set up a smaller MD simulation with slower cooling and heating rates. Specifically, we start with 8,000 atoms in the zinc-blende (B3) phase of SiC at 5000 K, so that the crystal becomes a homogeneous liquid. A conservative simulation time step of 0.5 fs was selected due to the elevated temperatures and pressures, the short vibrational periods of light Si and C atoms, and the need to accurately capture rapid bond rearrangements during decomposition while minimizing integration error. We perform an equilibration for 0.5 ns at each temperature, followed by a 0.5 ns cooling process at a rate of 400 K/ns. We alternate between equilibration and cooling steps until reaching 3000 K, then we ramp the temperature back up to 5000 K following the same scheme. The temperature profile over simulation time is shown as the blue curve in Fig. 3b.

To identify spontaneous phase separation, we use the local C fraction (concentration) as the order parameter and track the size of the largest C cluster. At each time step, we divide the simulation cell into $10 \times 10 \times 10$ voxels and calculate the C atom fraction in each voxel. The population of voxels with different local fraction levels over time is represented by the color scale in Fig. 3a, with red indicating higher populations.

At the beginning of the simulation, at a pressure under 30 GPa and a high temperature of 5000 K, we observe a high population of 0.5 local C fraction values, indicating a homogeneous liquid with an equal mixture of Si and C atoms. Fig. 3b shows the system temperature and the largest C cluster size. As the system cools, the largest C cluster size increases, notably around 4000 K. At 7 ns, when the system cools down to 3600 K, spontaneous decomposition is complete, with C atoms mostly depleted from the Si liquid. The local C-fractions are either near 0 (Si-rich) or near 1 (C-rich), as indicated in the upper panel.

During heating, the reverse process initiates at the same transition temperature of approximately 4000 K. The C cluster dissolves into the Si liquid, and the local C fraction returns to around 0.5, analogous to the initial state of the simulation. This indicates that the system has returned to the homogeneous liquid state upon heating. Similar results are obtained for 60 GPa and 90 GPa, which are shown in the Supplementary Information Fig. S9. Having confirmed the reversibility, we proceed

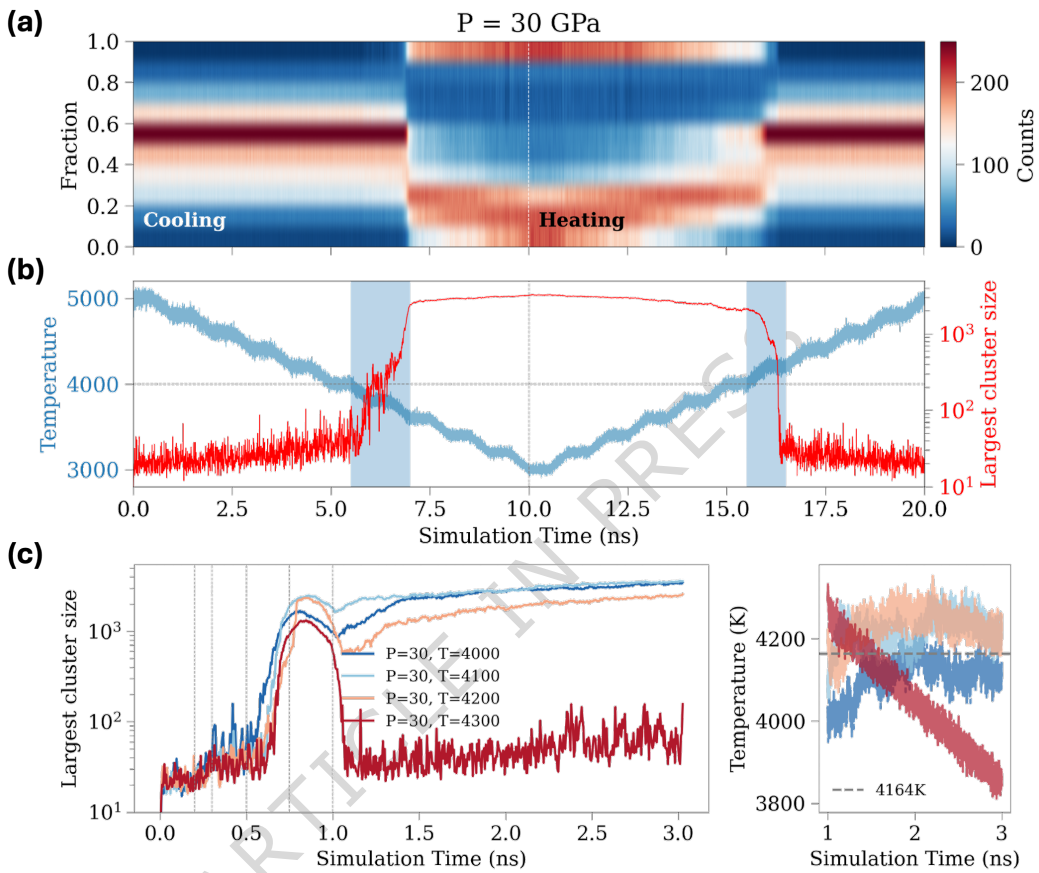

Figure 3: **SiC high-temperature phase transitions and two-phase coexistence simulations at 30 GPa.** (a) and (b) High-temperature phase transitions (liquid and decomposed phase boundary) from 8,000-atom cooling and heating simulations, illustrating the reversibility of phase transition. (a) Population distribution of local C atom fraction over simulation time: a single peak indicates the homogeneous liquid phase, while multiple peaks indicate the decomposed (Si+C) phase (red: high population, blue: low population, color bar represents voxel count, with a total population of 1,000 voxels). (b) Temperature (blue) and largest carbon cluster size (red, number of atoms) over simulation time, with blue shaded regions indicating the phase transition boundaries. (c) Two-phase coexistence simulations with 16,000 atoms, confirming the coexistence temperature by tracking the largest carbon cluster size (left) and temperature convergence at the NPH stage (right). Different colors represent trajectories cooling down to different estimated temperatures, T_{es}.

with a quantitative estimation of the transition temperature between the homogeneous liquid and decomposed Si + C phase, with a four-stage simulation protocol shown in Fig. 1c:

1. **Initial Equilibration:** The crystalline supercell is first melted and then cooled to the estimated transition temperature T_{es}. The entire cell is then equilibrated at this temperature to prepare the initial liquid phase.
2. **Interface Creation:** To create an interface, the positions and velocities of half the atoms in a slab along z-axis are fixed, while the other half is cooled further to a lower temperature, T_l (choosen here as 3500 K) to induce the formation of the decomposed phase.
3. **Interface Refinement:** The cooled region is heated back from T_l to T_{es} in the $NP_{zz}T$ ensemble. This action ensures a minimal thermal gradient across the cell while creating a stable interface between the decomposed phase and the liquid phase.
4. ***NPH* Coexistence:** Constraints are removed, and the entire system is equilibrated in the NPH ensemble. The phase boundary equilibrates, and the system temperature converges to the phase transition temperature.

The first three stages prepare the two-phase interface near the estimated transition point. During the final NPH stage, the system equilibrates. The temperature at which both phases coexist in equilibrium is then determined as the phase transition temperature.

As shown in Fig. 3c, the initial liquid phase at T_{es} is prepared after 0.5 ns (0.2 ns melting, 0.1 ns cooling, and 0.2 ns equilibration). Then, the decomposed phase is clearly formed during stages 2 and 3 (achieved by 0.25 ns of cooling followed by 0.25 ns of heating), indicated by the sharp increase in the size of the largest carbon cluster. Starting at the 1 ns mark, the system enters the final NPH coexistence stage and subsequently converges to a final transition temperature of 4164 K in the coexistence simulation. We note that for runs initialized with an estimated temperature of $T_{es} = 4300$ K, the temperature was too high to stabilize the decomposed phase, and temperature convergence was therefore not achieved. Thus, we computed the final average transition temperature from the remaining three converged runs. Additional two-phase simulation results for pressures at 45, 60, 70 GPa are provided in the Supplementary Information Fig. S10.

Low-temperature phase boundary: crystal ↔ decomposed Si+C

Next, we investigate the lower-temperature transition between the crystal (B1 or B3) phases and the decomposed phase. To overcome hysteresis and high nucleation barriers that prevent decomposition in direct MD simulations of B3 SiC crystals heated to 4000 K, we employ a similar four-stage two-phase coexistence simulation approach [31], as illustrated in Fig. 1c.

1. **Initial Equilibration:** Equilibrate the crystalline supercell at pressure P (10–90 GPa) and an initially estimated transition temperature T_{es}.
2. **Interface Creation:** Fix half of the z-slab, while melt the other half by heating it to high temperature $T_h \gg T_{es}$ in the $NP_{zz}T$ ensemble to induce the liquid phase.
3. **Interface Refinement:** The melted half is then cooled from T_h to T_{es} in the $NP_{zz}T$ ensemble. This process facilitates the formation of the decomposed phase while maintaining the unperturbed crystalline half, thus creating a stable crystal-decomposed interface.
4. ***NPH* Coexistence:** Constraints are removed, and the entire system is equilibrated in the NPH ensemble. The phase boundary equilibrates, and the system temperature converges to the phase transition temperature.

Each of the four stages is simulated for 0.5 ns, and the snapshots at the end of each stage are shown in Fig. 4 for the pressure values of 30 GPa (starting with B3 zinc blende) and 90 GPa (starting with B1 rock salt). In the last stage of the two-phase simulation where the interface is allowed to move, the temperature of the entire system fluctuates and converges to the actual transition temperature at which the decomposed and crystalline phases coexist in equilibrium, and the interface stops moving.

Fig. 5 shows the results of the heating and cooling process in the two-phase coexistence simulations for different initial temperatures near the expected transition temperature.

At the fixed pressure of 30 GPa, during the heating stage (0.5–1 ns), the heated half of the supercell becomes amorphous, and the overall fraction of zinc-blende local structures in the supercell decreases to 0.5. The C clusters begin to form during the cooling stage (1–1.5 ns) and continue growing in size at 1.5–2 ns as demonstrated in the second column of Fig. 5. In the NPH simulation

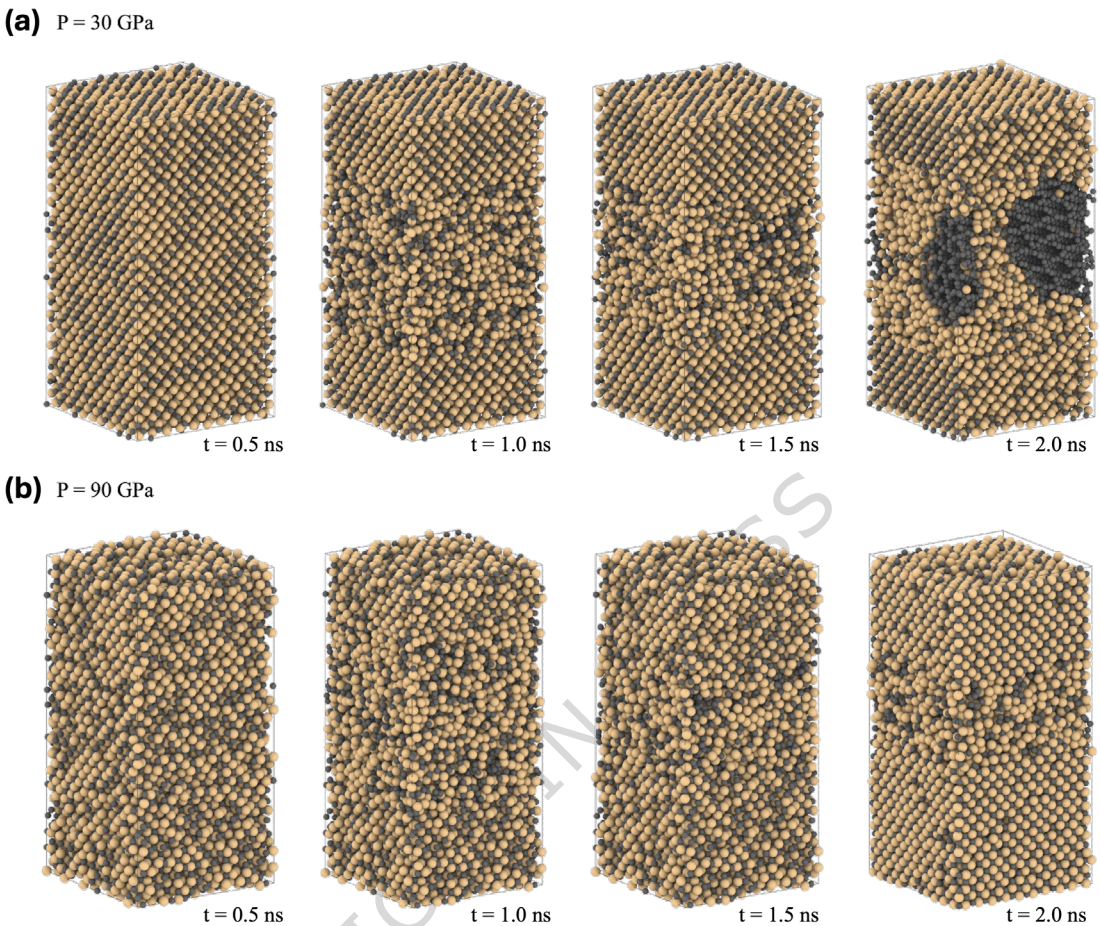

Figure 4: **Snapshots of two-phase coexistence simulations.** Snapshots of the four stages of the two-phase MD at 30 GPa (a) and 90 GPa (b) pressures. Each stage is simulated for 0.5 ns. Yellow: Si, black: C.

stage (1.5–2 ns), both B3 crystal and decomposed Si + C phases coexist, with relatively different equilibrated fractions depending on the initial temperature. Meanwhile, multiple simulations with different initial temperatures converge to approximately the same temperature during the NPH stage, which is identified as the transition temperature (shown in the third column of Fig. 5).

At 90 GPa, where the stable phase at low temperature is rock salt (B1), a similar procedure starting from the B1 phase yields a transition temperature around 4500 K. Notably, the carbon cluster sizes formed at 90 GPa are much smaller than those at 30 GPa, leading us to conjecture that at sufficiently high pressures, the decomposed Si+C phase between the crystalline and liquid phases may not be present. Additional coexistence simulations were performed for the B3 phase (at 10, 20, 45, 60, 70, and 80 GPa) and the B1 phase (at 85 and 100 GPa). In addition, we investigated finite-size effects

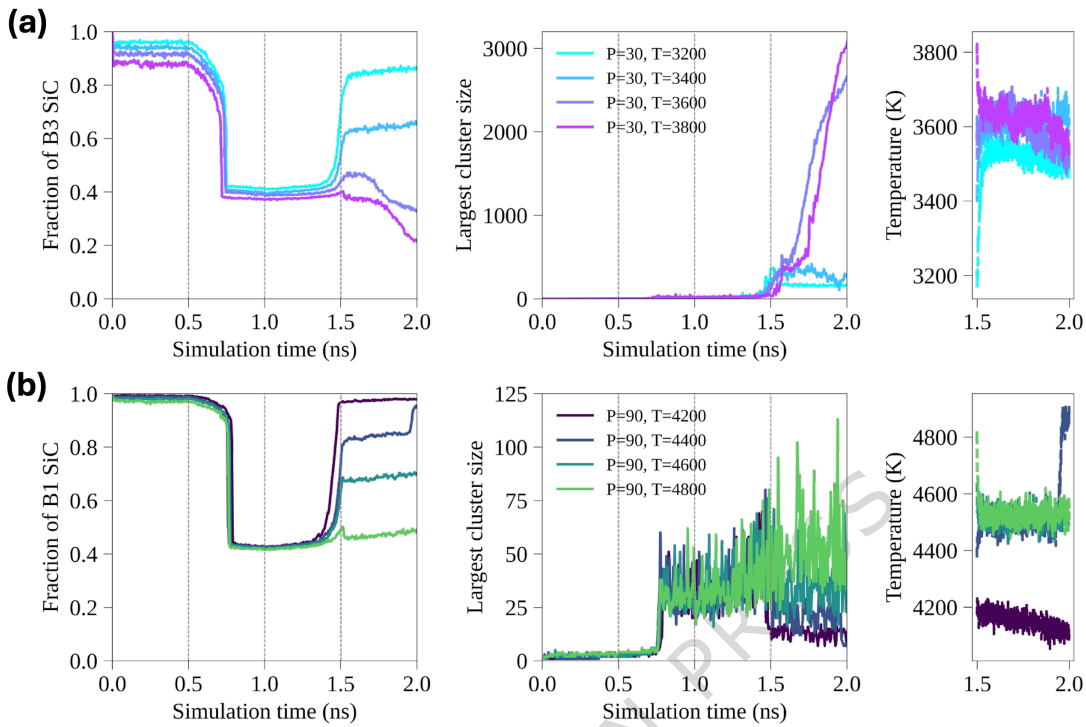

Figure 5: **Quantitative analysis of two-phase coexistence simulations.** (a) Simulations at 30 GPa starting from the zinc-blende phase. (b) Simulations at 90 GPa starting from the rock-salt phase. Panels from left to right show the time evolution of the fraction of crystalline (zinc-blende or rock-salt) structures, the size of the largest carbon cluster, and the temperature convergence during the final NPH stage. Different colors represent trajectories initialized with different estimated temperatures, T_{es}.

by performing significantly larger simulations (4x and 8x the original size). These results and the details for determining the final phase transition temperatures are presented in the Supplementary Information Figs. S12, S13, and S15.

Phase diagram

Finally, we combine the results obtained from the MD simulations of the SiC phase transitions into a complete pressure-temperature phase diagram. Fig. 6 presents the P-T diagram, illustrating the B3 $\leftrightarrow$ B1, B3 $\leftrightarrow$ gas, B3 $\leftrightarrow$ Si + C, B1 $\leftrightarrow$ Si + C, and Si + C $\leftrightarrow$ SiC (liquid) transitions. For completeness, we briefly describe the simulations of B3 $\leftrightarrow$ B1 transition and B3 $\leftrightarrow$ gas below, although these are not the primary focus of this work.

The B3 $\leftrightarrow$ B1 transition pressures at various temperatures are determined using the same methods as in our previous work [32]. Starting with the B3 crystal, we increase pressure at a fixed temperature to generate a configuration containing both phases. Then, we perform constant-pressure MD simulations on these coexistence structures at different pressures to identify the transition point, characterized by the stable coexistence of the two phases. The pressure scan results are shown in the Supplementary Information Fig. S17. The B3 $\leftrightarrow$ B1 transition pressures identified from our simulations (along pink-blue boundary in Fig. 6) are close to experimental measurements with a deviation of less than 20 GPa.

At zero or low pressure, the SiC B3 crystal sublimates into the gas phase instead of melting, which occurs only under high pressure. Our NPT MD simulations at P = 0–15 GPa and T = 3900–4500 K reveal a qualitative pressure threshold between 5 and 10 GPa: at lower pressures (0, 1, and 5 GPa), sustained volumetric expansion above 4000–4200 K indicates progressive sublimation to a gas/vapor phase (details in Supplementary Information Fig. S18). While our simulations identify this sublimation threshold, most experimental literature at low pressure focuses on sublimation growth conditions rather than on establishing the equilibrium solid-gas phase boundary. An earlier study [33] reported a sublimation temperature-pressure relationship, but it did not distinguish between the specific solid phases of SiC.

Regarding the transition between condensed phases, there is a qualitative disagreement among experiments: Hall [13] and Sokolov [14] report congruent melting, whereas Daviau *et al.* [9] and five earlier independent studies (Bhaumik *et al.* [10, 11], Dolloff [12], Togaya [8], Ekimov *et al.* [7]) observe incongruent decomposition—consistent with our simulations. Quantitatively, at 10 GPa, our predicted decomposition temperature falls within the cluster formed by those five independent measurements, supporting our placement of the boundary there. At higher pressures, however, our values are substantially above the laser-heated DAC series from Daviau *et al.* [9] (blue-orange circles). This laser-heated DAC dataset shows several inconsistencies. When extrapolated downward, it sits discontinuously below the lower-pressure data. It also shows internal inconsistency with a separate study by the same group [34] (blue triangles). Furthermore, it conflicts with other

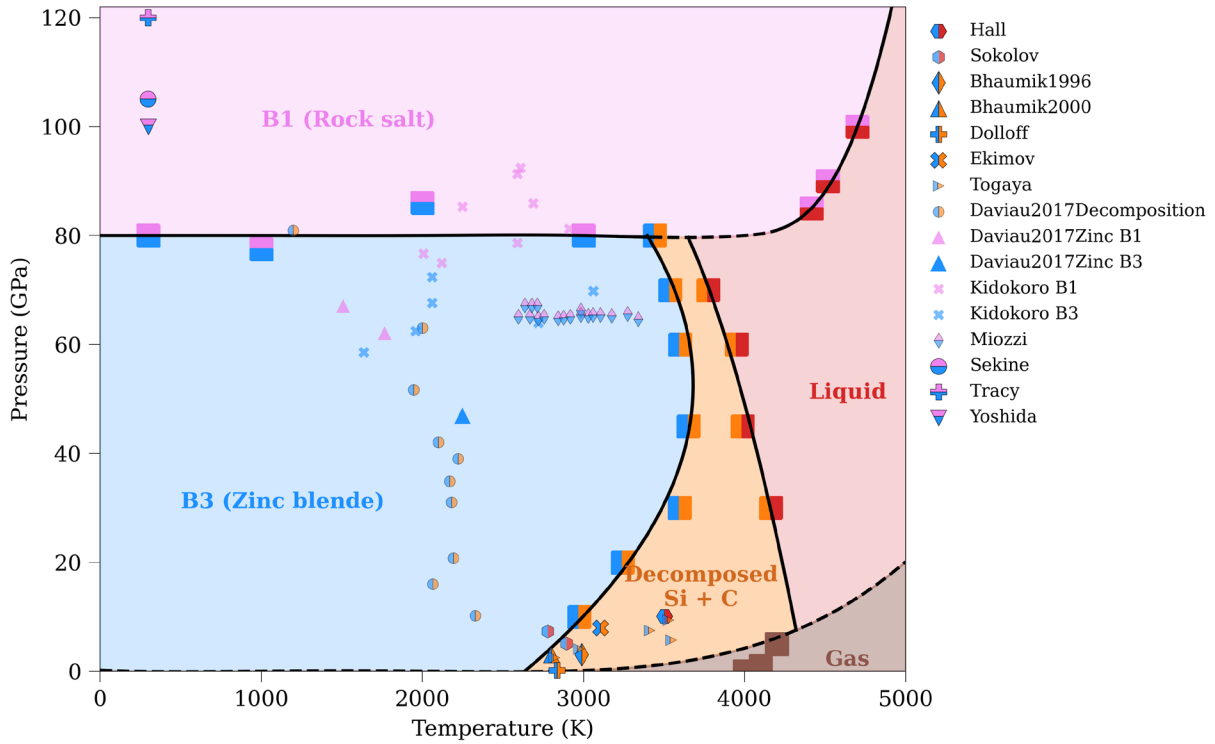

Figure 6: **Phase diagram of SiC.** Results from our MD simulations are denoted in big squares, and the inferred phase boundaries are drawn with black solid lines (interpolated) and dash lines (extrapolated). Blue: B3 (ZB), pink: B1 (RS), orange: decomposed Si + C, red: homogeneous liquid, brown: gas. The background colors indicate the stability regions of different phases inferred by our simulations. Experimental reports of congruent melting (blue-red symbols): hexagons [13], rotated hexagons [14]. Incongruent melting (blue-orange symbols): diamonds [10], triangles [11], pluses [12], crosses [7], left-pointing triangles [8], circles [9]. B3-B1 transition (blue-pink): triangles [34], crosses [35], diamonds [36], circles [37], pluses [38], inverted triangles [39].

B3-B1 studies [35, 36] (blue cross and pink-blue diamonds) that report stable B3-SiC in a region where Daviau *et al.* claimed decomposition occurs. Together with the broader scatter among datasets, this indicates that the high-pressure decomposition boundary remains experimentally underconstrained. Potential sources for these discrepancies, such as temperature gradients and transients in the DAC environment, highlight the need for further high-pressure measurements to resolve these conflicts.

The high-temperature phase boundary is close to the melting point of graphite and diamond carbon, indicating that the C clusters dissolve at around 4000 K and SiC becomes a homogeneous liquid

mixture. As depicted in Supplementary Information Fig. S3, the Si-C peak indicates that the Si and C are mixed well, and the complete phase separation does not occur, as opposed to the RDF shown in Fig. 2c.

Discussion

Our MLFF, based on Gaussian process regression [40], provides uncertainty estimations for its predictions. To ensure the fidelity of our large-scale MD simulations, we assess whether high-uncertainty configurations are involved. A sufficient training dataset covering a variety of configurations results in low uncertainties during simulations, as the model is familiar with the encountered atomic structures. Conversely, high model uncertainty implies the MD has proceeded to configurations not covered by the training data, potentially reducing prediction reliability. Therefore, we evaluate the model uncertainty on snapshots from the decomposition MD simulations. As shown in Supplementary Information Fig. S16, the model uncertainty remains well below the acquisition threshold of our force field active learning workflow. This indicates that our collected training data set sufficiently covers the configuration space, ensuring a high confidence level in the model predictions.

In our MD simulation where decomposition occurs, we cannot directly model the transition from a pure crystalline B3 phase to the decomposed phase due to hysteresis and nucleation barriers. Instead, we must overheat and amorphize the crystalline SiC to a homogeneous liquid before decomposition can take place during the cooling stage. Meanwhile, experimental observations align with this approach, demonstrating that the decomposition originates from the heating and cooling processes. For example, Daviau and Lee reported no evidence of decomposition in the Raman spectra when heating to 3200 K at 81 GPa. However, the surrounding region, annealed to 1200 K, showed D and G band signatures of carbide-derived carbon [9]. Similarly, Togaya and Sugiyama [8] reported using a sample quenched from a molten state to determine the onset of fusion, further supporting the importance of cooling in the decomposition process.

While numerous experiments have confirmed the occurrence of incongruent melting or decomposition in SiC, some studies have reported congruent melting. Considering the slow kinetics of SiC decomposition and phase transformation, the grain size can influence the process. For instance, in experiments reporting congruent melting, large single crystalline grains (between 150 μm and 3 mm) are used, which likely hinders the transition [14].

While our MD simulations confirm incongruent melting at various pressures, qualitatively consistent with Daviau *et al.* [9], our obtained transition temperatures at high pressures are significantly higher than the reported measurements around 2000 K. One limitation of our MLFF is that it is trained primarily on high-temperature/high-pressure data, focusing on bulk solid-solid and solid-liquid transitions, but is not optimized for simulating surfaces or capturing detailed effects across a wide range of complex crystalline defect ensembles. The expressive power of the MLFF and the accuracy of DFT can contribute to the discrepancy of our simulation results with experiments. More expressive and expensive MLFF models such as the equivariant neural networks [41, 42] can be used to potentially improve the accuracy.

On the other hand, the discrepancy may also be attributed to several factors in experimental setups: (1) Since the temperature is measured via thermal emission from the surface, the approach could underestimate the core temperature. (2) The heat distribution in the sample could be inhomogeneous, such that overheating in certain regions might facilitate the decomposition at lower apparent temperatures. Although there are no other experimental reports at such high pressures, our simulation is in good agreement with the transition temperature at a lower pressure of 10 GPa found in five other experiments (Bhaumik *et al.* [10, 11], Dolloff [12], Togaya [8], and Ekimov *et al.* [7]). We also note that in other applications, such as physical vapor deposition growth of SiC, a temperature of $\sim$ 2500 K is used at $\sim$ 0 GPa, demonstrating SiC's stability at temperatures higher than 2000 K [43]. This observation further supports the plausibility of our higher predicted transition temperatures at elevated pressures.

The two-phase coexistence MD simulation creates an interface between two different phases and thereby overcomes the nucleation barrier. It is possible that the defect concentration influences the

phase transition temperature. Even state-of-the-art epitaxially grown SiC wafers have high defect densities [43]. Therefore, we performed additional simulations, in which we introduce different point defect concentrations in the crystal. As shown in Supplementary Information Fig. S14, the concentration of defects does not have a significant influence on the transition temperature determined by the two-phase MD simulation. Macroscopic defects such as dislocations and phase boundaries could have a greater impact than point defects but are out of the scope of this study. Besides point defects, we further note that free surfaces or high surface-to-volume ratios, absent from our periodic bulk simulations, can modify local coordination, provide heterogeneous nucleation sites, and shift the decomposition/melting temperature, and thus may contribute to remaining experiment–simulation discrepancies.

While some previous computational studies using empirical and neural network potentials obtain amorphous SiC through melting and quenching [21, 22], our simulations show that the melting and quenching process results in the decomposition of SiC. Instead, techniques such as irradiation are required for the amorphization of SiC, which is consistent with most experiments [44].

Building upon our findings on SiC decomposition, we now explore possible mechanisms underlying this process. The two primary mechanisms to consider are nucleation and spinodal decomposition. To investigate spinodal decomposition, we calculated the C-C spatial correlation function from local concentrations (Supplementary Information Fig. S8). Notably, towards the end of the cooling process, particularly below 3400 K, a peak appears at approximately 40 Å. This implies periodic fluctuations in the carbon concentration, indicative of a wavelength of the phase separation mode [45, 46]. This observation aligns with the spinodal decomposition mechanism reported in alloy systems [45, 46] and is consistent with a recent tight-binding MD study of SiC under tensile stresses [47]. To analyze the nucleation of solid carbon clusters during decomposition, we tracked the evolution of diamond and graphite clusters. Fig. 7 illustrates the various stages of carbon cluster development, highlighting their transformation into either diamond or graphite phases. We applied cluster analysis in OVITO [29] with a 1.55 Å cutoff, approximately the bond length in graphite and diamond, to identify clusters. The formation of different phases was analyzed by the

"identify diamond structure" method [48] for diamond, and polyhedral template matching [28] for graphite. We track the evolution of clusters by identifying those with the largest overlap with the final structures at each time step. As shown in Fig. 7, in earlier stages, small nuclei lack clear lattice symmetry or phase identity. For graphite, the hexagonal structure can be traced back to smaller clusters. However, tracking becomes challenging for clusters below 100 atoms, as dynamic rearrangements reduce the overlap ratio quickly over time for both diamond and graphite structures. Detailed enthalpy calculations quantifying the thermodynamic driving force for phase separation are provided in Supplementary Information Fig. S19 and S20.

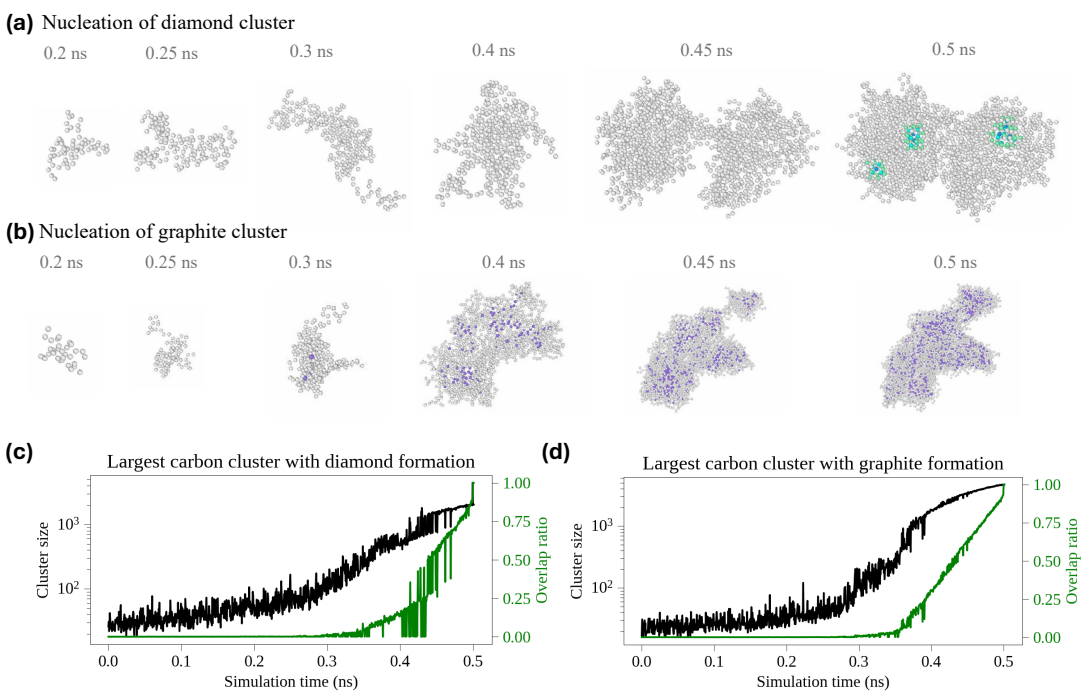

Figure 7: **Nucleation analysis of carbon clusters from 512,000-atom simulations.** (a) Nucleation of diamond cluster at 60 GPa. Diamond core is colored in cyan. (b) Nucleation of graphite cluster at 30 GPa. Graphite core is colored in purple. Increase of the diamond cluster (c) and graphite cluster (d) size (colored in black) and its overlap (colored in green) with the final largest cluster, with simulation time.

In conclusion, our machine learning molecular dynamics study confirms the occurrence of incongruent melting in SiC, with the decomposition of SiC into Si and C being observed at a temperature range of 3000–3600 K at high pressures. We also identified a transition at higher temperatures where the decomposed phase transforms into a homogeneous liquid phase. The highly efficient

and accurate MLFF enabled previously intractable modeling and simulation of the decomposition process, overcoming limitations of both *ab initio* or empirical force fields in terms of computational cost and accuracy. Our MD simulations provide atomic-level insights, revealing nucleation mechanisms and process details inaccessible in experiments. These findings support the existence of incongruent melting at high pressure, clarifying controversial experimental observations. In summary, our study provides a comprehensive understanding of SiC melting and decomposition behavior, along with a complete phase diagram, reconciling and extending previous experimental and theoretical work in this field.

Methods

Machine learning force field

Accurately modeling the melting and decomposition of SiC at high temperature and pressure requires an interatomic potential that captures complex bonding environments, including phase separation. Traditional empirical force fields can reproduce certain crystalline and shock-response properties. For example, Tersoff [19] and Vashishta [17] potentials have been applied in planar and impact shock studies of SiC [49, 50, 51]. However, the concurrent bond breaking, chemical partitioning, and long-timescale phase coexistence needed to delineate the high-P / high-T decomposition boundary remains challenging for such potentials. While AIMD [15, 16] provides accurate atomic forces, its high computational cost limits simulations to small system sizes and short timescales. To overcome these challenges, we employ a MLFF trained on DFT calculations, such that the atomic interactions can be modeled with high accuracy, while remaining cost effective for large-scale simulations.

Among general MLFF frameworks [41, 42, 52, 53], FLARE was selected because: (i) Bayesian uncertainties focus acquisition on novel crystal, liquid, and early segregation environments, enabling highly efficient collection of non-redundant data; (ii) sparse GP to polynomial mapping yields high simulation efficiency at the 10^4–10^6 atom scale needed for multi-temperature/pressure coexistence runs; (iii) reuse of a previously validated SiC setup [32] ensures methodological continuity. More

expressive deep equivariant models could lower force errors at substantially higher cost, a trade-off we reserve for future refinements.

Our MLFF is built using the FLARE framework [26, 32], which is based on a sparse Gaussian process (SGP) model [40] with atomic cluster expansion descriptors [54]. This model predicts forces while providing uncertainty quantification.

Bayesian active learning

To efficiently generate training data, we employ Bayesian active learning, which systematically selects new atomic configurations where the MLFF is most uncertain. The workflow follows these steps: (1) Initial Training: The MLFF is first trained on a small set of DFT-calculated structures, including perfect and slightly perturbed crystal structures. (2) Uncertainty-Guided MD: The MLFF runs MD simulations, predicting atomic forces while simultaneously estimating its uncertainty. (3) Selective DFT Calculations: If the model's uncertainty exceeds a threshold, new configurations are labeled using DFT. Otherwise, continue with MD. (4) Iterative Refinement: The MLFF is retrained with the newly acquired DFT data, progressively improving its accuracy. This adaptive learning process ensures that the force field is only trained where necessary, avoiding redundant DFT calculations while capturing the relevant phase space.

Once the active learning is complete, we map the SGP into an equivalent but more computationally efficient polynomial model [32, 40], which serves as the final MLFF for large-scale production simulations in LAMMPS [55]. The DFT calculations are performed using VASP [56] with the PBE exchange correlation functional [57], following the computational settings in our previous works [32, 58].

The initial training set contains SiC polymorph data from our previous study [32], encompassing the hexagonal 2H, 4H, and 6H polytypes, B3 (zinc blende or 3C) and the high-pressure B1 (rock salt) phases. We then employ the FLARE Bayesian active learning workflow to systematically sample data that captures melting and decomposition behavior SiC across a wide pressure range. Active learning MD simulations are performed for a 64-atom SiC supercell at 0, 30, 60, 90, and 120 GPa

over a temperature range of 2000–6000 K until melting is observed. In addition, active learning for a 512-atom SiC supercell is conducted at 5000 K across the same pressure range. To enhance our data coverage for the decomposition products, additional data is collected for pure carbon (diamond and graphite phases, 2000–4000 K) and pure silicon (1000–3000 K) across all pressure conditions.

The final trained MLFF is then used to investigate SiC melting and decomposition under high temperature and pressure conditions through two-phase coexistence simulations, which allowed for the accurate determination of phase transition temperatures.

Large-scale molecular dynamics simulation

The large-scale MD simulations are conducted using GPU-accelerated LAMMPS [55] with Kokkos parallelization [59] and the FLARE MLFF pairstyle, which has demonstrated exceptional performance in billion-atom catalytic simulations [60]. During the melting simulations, the NPT ensemble with anisotropic (`aniso`) control of cell dimensions is employed, allowing independent scaling along the x, y and z directions through stress components P_{xx}, P_{yy}, and P_{zz}. Phase separation exhibits a tendency to minimize the interface between decomposed phases, necessitating anisotropic elongation of the supercell, as illustrated in Fig. 2.

Code Availability

Post-processing scripts are available on Github: https://github.com/YuuuXie/SiC_MLMD_phase_diagram. For the machine learning force field, this work utilizes FLARE (version 1.3.0) for training and deployment, available at https://github.com/mir-group/flare.

Data Availability

The data and scripts are available on Zenodo: https://doi.org/10.5281/zenodo.14648292 and https://doi.org/10.5281/zenodo.15066527.

Acknowledgement

We acknowledge Cameron Owen and Anders Johansson for discussions and help with large simulation setup and computational resources. We acknowledge Evelyn Hu for helpful discussions and feedback.

Y.X. is supported by the "Design & Assembly of Atomically-Precise Quantum Materials & Devices" grant DE-SC0020128 of the Department of Energy. M.W. is supported by the National Science Foundation, Office of Advanced Cyberinfrastructure (OAC), under Award No. 2118201. B.K. and F.S. are supported by the Harvard University Materials Research Science and Engineering Center funded by the National Science Foundation grant DMR-2011754. The simulation and analysis are done on the Harvard Cannon cluster. This research used resources of the National Energy Research Scientific Computing Center (NERSC), a DOE Office of Science User Facility supported by the Office of Science of the U.S. Department of Energy under Contract No. DE-AC02-05CH11231 using NERSC award BES-ERCAP0024206.

Competing interests

The authors declare no competing financial or non-financial interests.

Author Contributions

Y.X. initiated the project, performed the training of the ML force field, phase transition simulations and post analysis. M.W. contributed to the dataset and code preparation, phase transition simulations and post analysis. S.R. contributed to the DFT settings, and the collection of experimental results. F.S. guided the analysis of nucleation and decomposition. B.K. supervised all aspects of the project. All authors contributed to the writing of the manuscript.

References

[1] Madar, R. Silicon carbide in contention. *Nature* **430**, 974–975 (2004).

[2] Madhusudhan, N., Lee, K. K. & Mousis, O. A possible carbon-rich interior in super-earth 55 cancri e. *Astrophys. J. Lett.* **759**, L40 (2012).

[3] Katoh, Y. & Snead, L. L. Silicon carbide and its composites for nuclear applications–historical overview. *Journal of Nuclear Materials* **526**, 151849 (2019).

[4] Matsunami, H. & Kimoto, T. Step-controlled epitaxial growth of sic: High quality homoepitaxy. *Materials Science and Engineering: R: Reports* **20**, 125–166 (1997).

[5] Yi, J., He, X., Sun, Y. & Li, Y. Electron beam-physical vapor deposition of sic/sio2 high emissivity thin film. *Applied surface science* **253**, 4361–4366 (2007).

[6] Zhang, W. & Van Duin, A. C. Atomistic-scale simulations of the graphene growth on a silicon carbide substrate using thermal decomposition and chemical vapor deposition. *Chemistry of Materials* **32**, 8306–8317 (2020).

[7] Ekimov, E. *et al.* A high-pressure cell for high-temperature experiments in a toroid-type chamber. *Instruments and Experimental Techniques* **47**, 276–278 (2004).

[8] Togaya, M. & Sugiyama, S. Melting behavior of β-sic at high pressure. *The Review of High Pressure Science and Technology* **7**, 1037–1039 (1998).

[9] Daviau, K. & Lee, K. K. Decomposition of silicon carbide at high pressures and temperatures. *Phys. Rev. B* **96**, 174102 (2017).

[10] Bhaumik, S., Divakar, C., Mohan, M. & Singh, A. A modified high-temperature cell (up to 3300 k) for use with a cubic press. *Review of scientific instruments* **67**, 3679–3682 (1996).

[11] Bhaumik, S. Synthesis and sintering of monolithic and composite ceramics under high pressures and high temperatures. *Metals Materials And Processes* **12**, 215–232 (2000).

[12] Dolloff, R. T. & Sara, R. *Research study to determine the phase equilibrium relations of selected metal carbides at high temperatures*, vol. 60 (Aeronautical Systems Division, Air Force Systems Command, US Air Force, 1961).

[13] Hall, H. T. High temperature studies. *Bringham Young University: Provo, UT, USA* 36 (1956).

[14] Sokolov, P. S., Mukhanov, V. A., Chauveau, T. & Solozhenko, V. L. On melting of silicon carbide under pressure. *Journal of Superhard Materials* **34**, 339–341 (2012).

[15] Finocchi, F., Galli, G., Parrinello, M. & Bertoni, C. M. Microscopic struture of amorphous covalent alloys probed by ab initio molecular dynamics: Sic. *Physical review letters* **68**, 3044 (1992).

[16] Saiz, F. An ab initio study on liquid silicon carbide. *J Phys. Chem. Solids* **137**, 109204 (2020).

[17] Vashishta, P., Kalia, R. K., Nakano, A. & Rino, J. P. Interaction potential for silicon carbide: A molecular dynamics study of elastic constants and vibrational density of states for crystalline and amorphous silicon carbide. *J. Appl. Phys.* **101**, 103515 (2007).

[18] Tersoff, J. Modeling solid-state chemistry: Interatomic potentials for multicomponent systems. *Physical review B* **39**, 5566 (1989).

[19] Tersoff, J. Chemical order in amorphous silicon carbide. *Physical Review B* **49**, 16349 (1994).

[20] Yan, W., Gao, T., Guo, X., Qin, Y. & Xie, Q. Melting kinetics of bulk sic using molecular dynamics simulation. *Science China Physics, Mechanics and Astronomy* **56**, 1699–1704 (2013).

[21] Devanathan, R., Gao, F. & Weber, W. J. Atomistic modeling of amorphous silicon carbide using a bond-order potential. *Nucl. Instrum. Methods Phys. Res. B* **255**, 130–135 (2007).

[22] Kubo, A. & Umeno, Y. Machine-learning-based atomistic model analysis on high-temperature compressive creep properties of amorphous silicon carbide. *Materials* **14**, 1597 (2021).

[23] MacIsaac, M., Bavdekar, S., Spearot, D. & Subhash, G. A genetic algorithm trained machine-learned interatomic potential for the silicon–carbon system. *The Journal of Physical Chemistry C* **128**, 12213–12226 (2024).

[24] Liu, Y. *et al.* Deep learning inter-atomic potential for irradiation damage in 3c-sic. *Computational Materials Science* **233**, 112693 (2024).

[25] Ishimaru, M., Bae, I.-T. & Hirotsu, Y. Electron-beam-induced amorphization in sic. *Physical Review B* **68**, 144102 (2003).

[26] Vandermause, J. *et al.* On-the-fly active learning of interpretable bayesian force fields for atomistic rare events. *npj Comput. Mater.* **6**, 1–11 (2020).

[27] Xie, Y., Vandermause, J., Sun, L., Cepellotti, A. & Kozinsky, B. Bayesian force fields from active learning for simulation of inter-dimensional transformation of stanene. *npj Comput. Mater.* **7**, 1–10 (2021).

[28] Larsen, P. M., Schmidt, S. & Schiøtz, J. Robust structural identification via polyhedral template matching. *Modelling and Simulation in Materials Science and Engineering* **24**, 055007 (2016).

[29] Stukowski, A. Visualization and analysis of atomistic simulation data with ovito–the open visualization tool. *Modelling and simulation in materials science and engineering* **18**, 015012 (2009).

[30] Gayler, M. Melting point of high-purity silicon. *Nature* **142**, 478–478 (1938).

[31] Dozhdikov, V., Basharin, A. Y. & Levashov, P. Two-phase simulation of the crystalline silicon melting line at pressures from–1 to 3 gpa. *The Journal of Chemical Physics* **137**, 054502 (2012).

[32] Xie, Y. *et al.* Uncertainty-aware molecular dynamics from bayesian active learning for phase transformations and thermal transport in sic. *npj Computational Materials* **9**, 36 (2023).

[33] Krieger, F. J. The thermodynamics of the silicon carbide/silicon-carbon vapor system. Tech. Rep. (1968).

[34] Daviau, K. & Lee, K. K. Zinc-blende to rocksalt transition in sic in a laser-heated diamond-anvil cell. *Physical Review B* **95**, 134108 (2017).

[35] Kidokoro, Y., Umemoto, K., Hirose, K. & Ohishi, Y. Phase transition in sic from zinc-blende to rock-salt structure and implications for carbon-rich extrasolar planets. *American Mineralogist: Journal of Earth and Planetary Materials* **102**, 2230–2234 (2017).

[36] Miozzi, F. *et al.* Equation of state of sic at extreme conditions: New insight into the interior of carbon-rich exoplanets. *J. Geophys. Res. Planets* **123**, 2295–2309 (2018).

[37] Sekine, T. & Kobayashi, T. Shock compression of 6h polytype sic to 160 gpa. *Phys. Rev. B* **55**, 8034 (1997).

[38] Tracy, S. *et al.* In situ observation of a phase transition in silicon carbide under shock compression using pulsed x-ray diffraction. *Phys. Rev. B* **99**, 214106 (2019).

[39] Yoshida, M., Onodera, A., Ueno, M., Takemura, K. & Shimomura, O. Pressure-induced phase transition in sic. *Phys. Rev. B* **48**, 10587 (1993).

[40] Vandermause, J., Xie, Y., Lim, J. S., Owen, C. J. & Kozinsky, B. Active learning of reactive bayesian force fields applied to heterogeneous catalysis dynamics of h/pt. *Nature Communications* **13**, 5183 (2022).

[41] Batzner, S. *et al.* E (3)-equivariant graph neural networks for data-efficient and accurate interatomic potentials. *Nat. Commun.* **13**, 2453 (2022).

[42] Musaelian, A. *et al.* Learning local equivariant representations for large-scale atomistic dynamics. *Nat. Commun.* **14**, 579 (2023).

[43] Kimoto, T. Bulk and epitaxial growth of silicon carbide. *Progress in Crystal Growth and Characterization of Materials* **62**, 329–351 (2016).

[44] Snead, L., Zinkle, S., Hay, J. & Osborne, M. Amorphization of sic under ion and neutron irradiation. *Nuclear Instruments and Methods in Physics Research Section B: Beam Interactions with Materials and Atoms* **141**, 123–132 (1998).

[45] Zhou, J., Odqvist, J., Thuvander, M. & Hedström, P. Quantitative evaluation of spinodal decomposition in fe-cr by atom probe tomography and radial distribution function analysis. *Microscopy and Microanalysis* **19**, 665–675 (2013).

[46] Sarkar, S. K., Ray, D., Sen, D. & Biswas, A. Nucleation–growth versus spinodal decomposition in fe–cr alloys: An experimental verification by atom probe tomography and small angle neutron scattering. *Microscopy and Microanalysis* **29**, 437–450 (2023).

[47] Herrero, C. P., Ramírez, R. & Herrero-Saboya, G. Cubic silicon carbide under tensile pressure: Spinodal instability. *Chemical Physics* **573**, 112005 (2023).

[48] Maras, E., Trushin, O., Stukowski, A., Ala-Nissila, T. & Jonsson, H. Global transition path search for dislocation formation in ge on si (001). *Computer Physics Communications* **205**, 13–21 (2016).

[49] Li, W., Yao, X. & Zhang, X. Planar impacts on nanocrystalline sic: a comparison of different potentials. *Journal of materials science* **53**, 6637–6651 (2018).

[50] Branicio, P. S. *et al.* Shock-induced microstructural response of mono-and nanocrystalline sic ceramics. *Journal of Applied Physics* **123** (2018).

[51] Li, W., Yao, X., Branicio, P., Zhang, X. & Zhang, N. Shock-induced spall in single and nanocrystalline sic. *Acta Materialia* **140**, 274–289 (2017).

[52] Bartók, A. P. & Csányi, G. Gaussian approximation potentials: A brief tutorial introduction. *International Journal of Quantum Chemistry* **115**, 1051–1057 (2015).

[53] Thompson, A., Swiler, L., Trott, C., Foiles, S. & Tucker, G. Spectral neighbor analysis method for automated generation of quantum-accurate interatomic potentials. *Journal of Computational Physics* **285**, 316–330 (2015).

[54] Drautz, R. Atomic cluster expansion for accurate and transferable interatomic potentials. *Phys. Rev. B* **99** (2019).

[55] Thompson, A. P. *et al.* LAMMPS-a flexible simulation tool for particle-based materials modeling at the atomic, meso, and continuum scales. *Computer Physics Communications* **271**, 108171 (2022).

[56] Kresse, G. & Hafner, J. Ab initio molecular dynamics for liquid metals. *Physical review B* **47**, 558 (1993).

[57] Perdew, J. P., Burke, K. & Ernzerhof, M. Generalized gradient approximation made simple. *Physical review letters* **77**, 3865 (1996).

[58] Ramakers, S. *et al.* Effects of thermal, elastic, and surface properties on the stability of sic polytypes. *Phys. Rev. B* **106**, 075201 (2022).

[59] Trott, C. R. *et al.* Kokkos 3: Programming model extensions for the exascale era. *IEEE Transactions on Parallel and Distributed Systems* **33**, 805–817 (2022).

[60] Johansson, A. *et al.* Micron-scale heterogeneous catalysis with bayesian force fields from first principles and active learning. *arXiv preprint arXiv:2204.12573* (2022).